1·0 2·8 2·5
    5·0 3·15 2·2
    5·6
    6·3 3·5
1·1   2·0
    4·0
    4·5
            1·8
1·25 1·4 1·6

NATIONAL BUREAU OF STANDARDS
MICROCOPY RESOLUTION TEST CHART

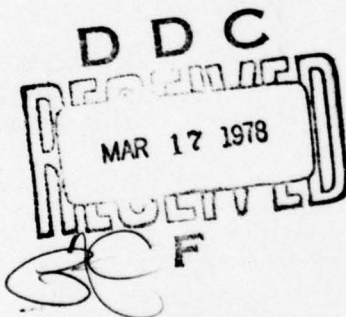NOSC TR 149

Technical Report 149

TURBULENT BOUNDARY LAYER WALL-PRESSURE FLUCTUATIONS ON AN AXISYMMETRIC BODY

HVL Patrick
7 September 1977

D D C

MAR 17 1978

F

Prepared For
Naval Sea Systems Command

Approved for public release; distribution unlimited.

**NAVAL OCEAN SYSTEMS CENTER
SAN DIEGO, CALIFORNIA 92152**

NOSC

NAVAL OCEAN SYSTEMS CENTER, SAN DIEGO, CA 92152

AN ACTIVITY OF THE NAVAL MATERIAL COMMAND

RR GAVAZZI, CAPT, USN
Commander

HL BLOOD
Technical Director

Released by
J. R. CAMPBELL, Head
Acoustic Research Division

Under authority of
M. O. HEINRICH, Head
Torpedo and Countermeasures
Department

REPORT DOCUMENTATION PAGE

READ INSTRUCTIONS
BEFORE COMPLETING FORM

1. REPORT NUMBER	2. GOVT ACCESSION NO.	3. RECIPIENT'S CATALOG NUMBER
NOSC/TR-149		

4. TITLE (and Subtitle)

TURBULENT BOUNDARY LAYER WALL-PRESSURE FLUCTUATIONS ON AN AXISYMMETRIC BODY

5. TYPE OF REPORT & PERIOD COVERED

Applied Research
June-September 1968

6. PERFORMING ORG. REPORT NUMBER

7. AUTHOR(s)

H. V. L. Patrick

8. CONTRACT OR GRANT NUMBER(s)

9. PERFORMING ORGANIZATION NAME AND ADDRESS

Naval Ocean Systems Center
San Diego, California 92152

10. PROGRAM ELEMENT, PROJECT, TASK AREA & WORK UNIT NUMBERS

Naval Ordnance Systems Command – Task Assignment UF 17 331-302

11. CONTROLLING OFFICE NAME AND ADDRESS

Naval Sea Systems Command
Washington, DC

12. REPORT DATE

7 September 1977

13. NUMBER OF PAGES

34

14. MONITORING AGENCY NAME & ADDRESS(if different from Controlling Office)

15. SECURITY CLASS. (of this report)

UNCLASSIFIED

15a. DECLASSIFICATION DOWNGRADING SCHEDULE

16. DISTRIBUTION STATEMENT (of this Report)

17. DISTRIBUTION STATEMENT (of the abstract entered in Block 20, if different from Report)

DDC
RECEIVED
MAR 17 1978
F

18. SUPPLEMENTARY NOTES

19. KEY WORDS (Continue on reverse side if necessary and identify by block number)

Wall pressure fluctuations
Buoyancy propelled vehicles
Flat plates
Rotating cylinders
Pipe flow
Axisymmetric bodies

20. ABSTRACT (Continue on reverse side if necessary and identify by block number)

A buoyancy propelled, fin-stabilized vehicle with a favorable pressure gradient over a major portion of its length was tested at Lake Pend Oreille, Idaho. Turbulent boundary layer wall-pressure fluctuations were measured at numerous locations of the body. In the region of favorable pressure gradient, the normalized wall-pressure spectral density was found to be similar to that on a flat plate. Transition from laminar to turbulent boundary layer flow occurred on the 30-inch-maximum diameter vehicle at transition-length Reynolds numbers as large as 9.2 million.

DD FORM 1473 EDITION OF 1 NOV 65 IS OBSOLETE
1 JAN 73

iii

393 159

CONTENTS

1

SYMBOLS USED IN THE TEXT

C_D	drag coefficient (D/q)
C_f	friction coefficient (τ_w/q)
D	drag
d	transducer diameter
dp/dx	pressure gradient
G	shape factor based on the velocity-defect profile $(2/C_f)^{1/2}(1-1/H)$
H	boundary layer shape factor $(\delta*/\theta)$
$\overline{p^2}$	mean square pressure $\left[\int_0^\infty \Phi(\omega)d\omega\right]$
q	free-stream dynamic pressure $\left(\rho U_\infty^2/2\right)$
R_ℓ	Reynolds number based on body length $(U_\infty \ell/\nu)$
R_x	transition Reynolds number $(U_\infty x/\nu)$
R_θ	Reynolds number based on momentum thickness $(U_\infty \theta/\nu)$
S	body surface area
u	local mean speed
U_∞	free-stream speed
u_τ	friction speed $(\tau_w/\rho)^{1/2}$
x,y	longitudinal and lateral space coordinates
β	pressure gradient parameter $[(\theta/\tau_w)(dp/dx)]$
δ	boundary layer thickness
$\delta*$	boundary layer displacement thickness $\left\{\int_0^\delta [1-(u/U_\infty)]\,dy\right\}$
θ	boundary layer momentum thickness $\left\{\int_0^\delta (u/U_\infty)[1-(u/U_\infty)]\,dy\right\}$
ν	kinematic viscosity
π	pressure gradient parameter $[(\delta*/\tau_w)(dp/dx)]$
ρ	fluid density
τ_w	wall shear stress
$\Phi(\omega)$	spectral density of wall-pressure fluctuations
ω	circular frequency

INTRODUCTION

Knowledge of the wall-pressure fluctuations beneath turbulent boundary layers is desirable because of the need to understand and reduce aerodynamically and hydrodynamically generated noise. A typical example is the background noise detected by a ship which is generated on and/or by the dome. All or part of this noise could be generated directly by the turbulent boundary layer flow and/or by the wall-pressure fluctuations that excite the dome structure. This in turn would generate its own pressure and acoustical noise field.

The buoyancy propelled vehicles used in these tests were developed primarily as high-speed (90 frames per second) and quiet test platforms to measure turbulent boundary layer wall-pressure fluctuations and radiated noise. Studies were intended to review the relationships between these physical phenomena and sonar dome structures and the resultant noise sensed by the sonar transducer.

Many detailed investigations have been performed on the fluctuating wall-pressure field beneath turbulent boundary layers in Newtonian fluids.[1,2,3,4,5,6,7,8,9] These studies were performed with flat plates in air,[1,2,3] rotating cylinders in water,[4,5] pipe flow in air[6] and water[7] and axisymmetric bodies in water.[8,9]

The effect of pressure gradients on the fluctuating wall-pressure field is of primary interest because of the known large effect of finite pressure gradients on turbulent boundary layer characteristics.[10] Schloemer[1] has shown that normalized $\Phi(\omega)$ can be greatly affected by certain favorable and unfavorable pressure gradients.

EXPERIMENTAL APPARATUS AND PROCEDURE

BUOYANCY-PROPELLED VEHICLES

The 30-inch-maximum-diameter laminar flow vehicle CARROT is a NACA 66-025 body of revolution ($\ell/d=4$), as shown in Figure 1. For the experiment a 5-inch-diameter aluminum boom, which contained the drag brake and supported four magnesium stabilizing fins, was attached to the magnesium body. The brake consisted of four sections which can be seen in Figure 1 in a partially deployed position. These sections were connected to a depth-sensitive cylinder and dynamic damping device via stainless steel cables. At a given distance below the surface, the brake was made to deploy, resulting in very low water-exit speeds.

The waviness of the vehicle's surface was low, though not measured. The surface was smoothed to approximately a 10-microinch (root mean square) finish. The painted body was hand rubbed with polishing compound and waxed. The first visible joint was at $x/\ell = 65$ percent, while hydrodynamically smooth joints existed at x/ℓ of 30 percent and 45 percent ($\ell = 120$ inches).
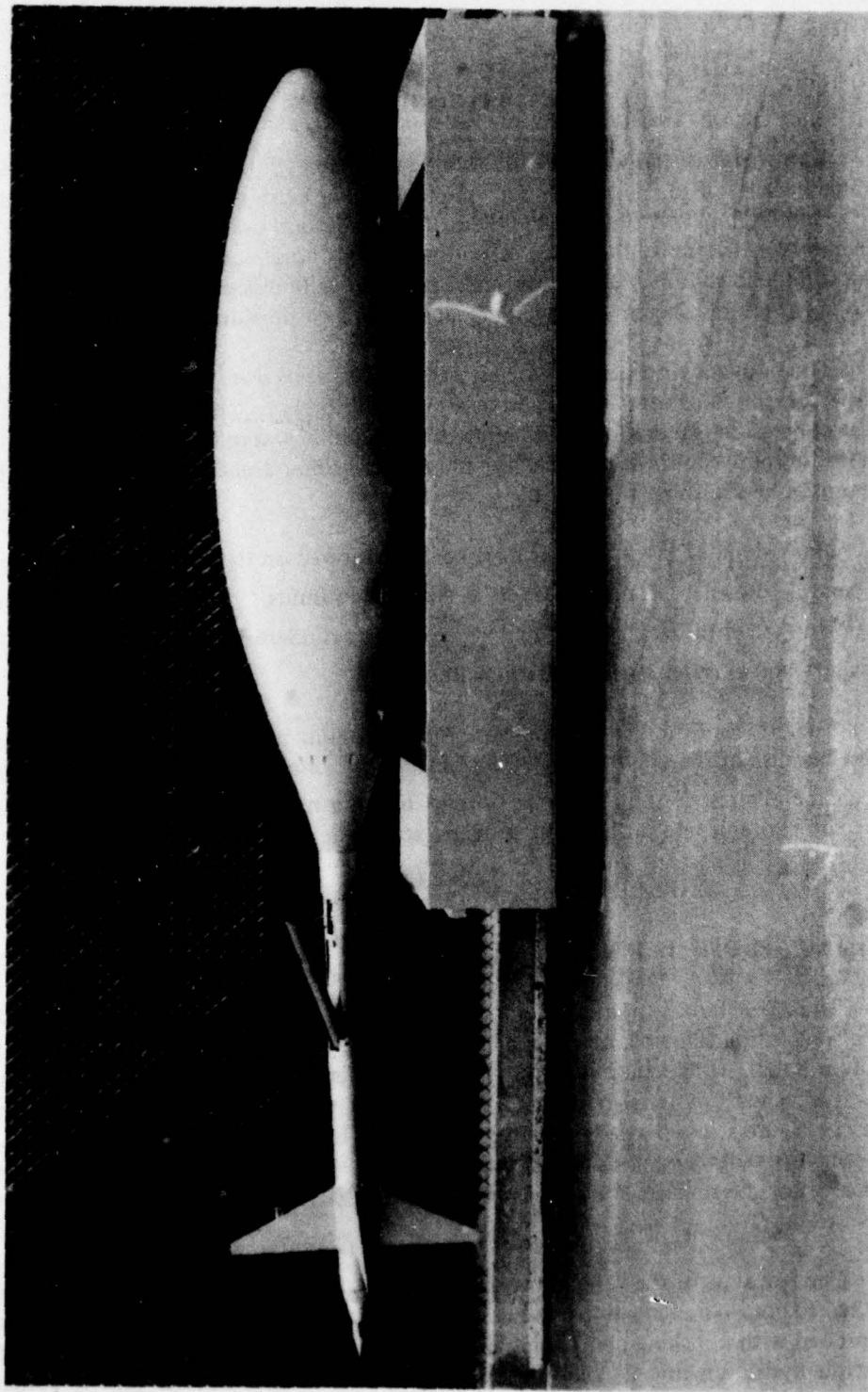
3

Figure 1. Laminar flow vehicle (CARROT), 30-inch-maximum diameter.

4

The 15-inch-diameter SWISH vehicle is shown in Figure 2. The magnesium torpedo had a length-to-diameter ratio of approximately 11, a modified ellipsoidal noise (7.5-inch-diameter flat disk with a 4-to-1 ellipsoidal fairing), a cylindrical midbody 6.6 diameters in length and was stabilized with four fixed fins. The surface of the vehicle was painted and smoothed to approximately 30-microinch (root mean square) finish. Joints and fastener heads, which allowed installation of the instrumentation package and lead ballast, were filled with epoxy automobile body putty.

Lead rings weighing approximately 50 pounds each were carried internally at the joint rings and were used to vary the buoyancy of both vehicles.

TEST PROCEDURE

A cable attached to the afterbody of the vehicle was connected to a motor-powered winch located on a barge at the test site. The cable passed through a pulley connected to a large concrete anchor on the lake bottom. The approximate vehicle depth was determined from a cable counter mounted on the barge.

Two men used a small boat to float the vehicle out to a position above the anchor. They attached the vehicle to the release mechanism on the small buoy and the vehicle was then pulled down to the correct depth. When the surrounding vicinity was acoustically quiet, i.e., when there were no motor-driven boats in the area, the acoustical command signal was executed on the barge and the vehicle was released.

Nominal release depth was approximately 500 feet; this depth usually allowed a reasonable period of run time at terminal speed before water exit. The mechanical release mechanism was actuated by a solenoid inside the vehicle. An electrical cable connected the vehicle and the small buoy attached to the pulldown cable. A receiving hydrophone and appropriate electronic circuitry were mounted in the buoy. At the appropriate time, an acoustical command signal generated from the barge actuated the relay in the buoy. This started the timer in the instrumentation package in the vehicle and, after a few seconds of delay, actuated the vehicle release mechanism.

During the run, the speed of the vehicle and the flush-mounted hydrophone signals were recorded on magnetic tape. A small propeller-type velocity meter attached to the leading edge of one of the stabilizing fins was used for measuring vehicle speed. The flush-mounted hydrophones were 1/8-inch-diameter barium titanate piezoelectric crystals. An ITHACO (Model 143M39) fixed-gain (20 dB) amplifier increased the volume of the signals, which were recorded on a PEMCO (Model 110) 14-channel magnetic tape recorder. The entire instrumentation package weighed approximately 50 pounds. Instrumentation and calibration details are presented in the Appendix.

VEHICLE DRAG

The theoretical[11] pressure distribution of the CARROT vehicle is shown in Figure 3. A favorable pressure gradient exists over a major portion of the body up to approximately $x/\ell = 58$ percent. Because of this favorable pressure gradient, it was possible to delay transition from laminar to turbulent boundary layer flow.[12,13] Carmichael[13] tested a
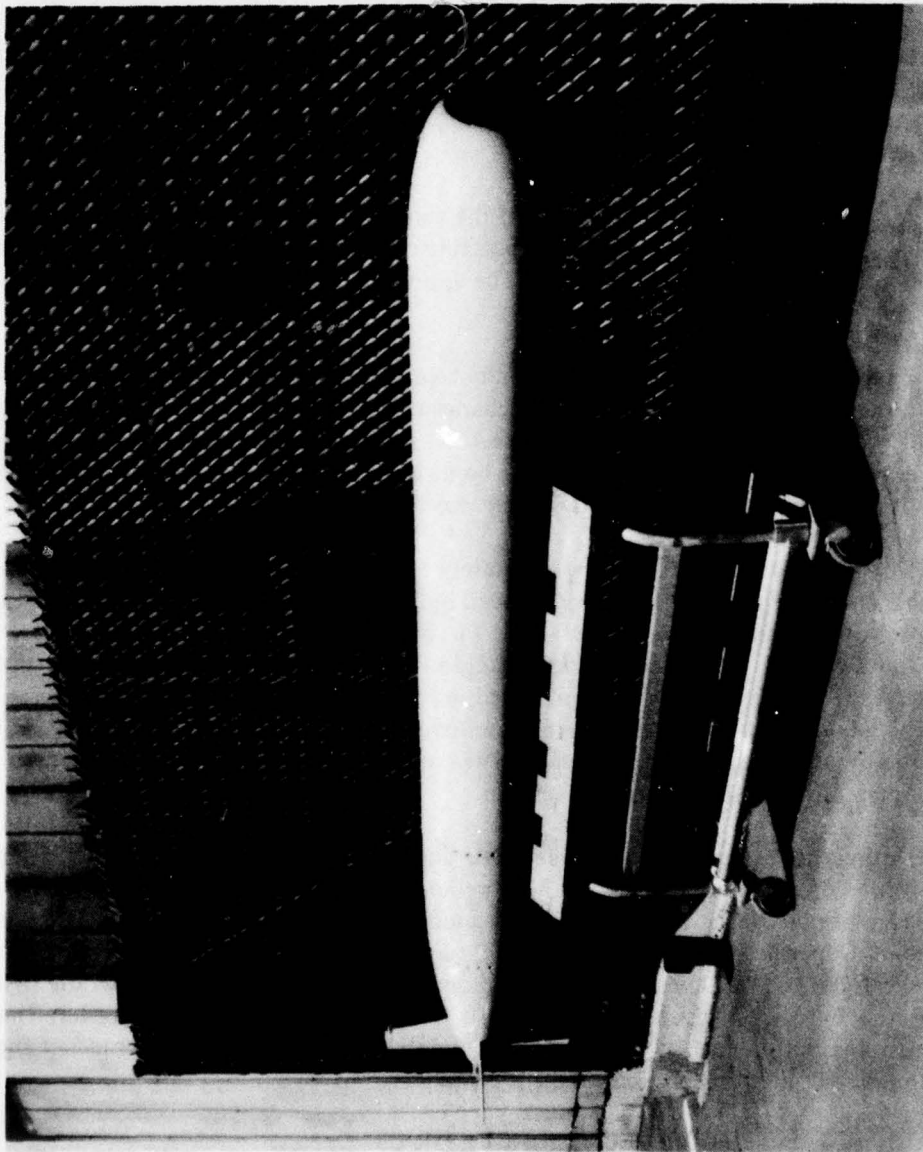
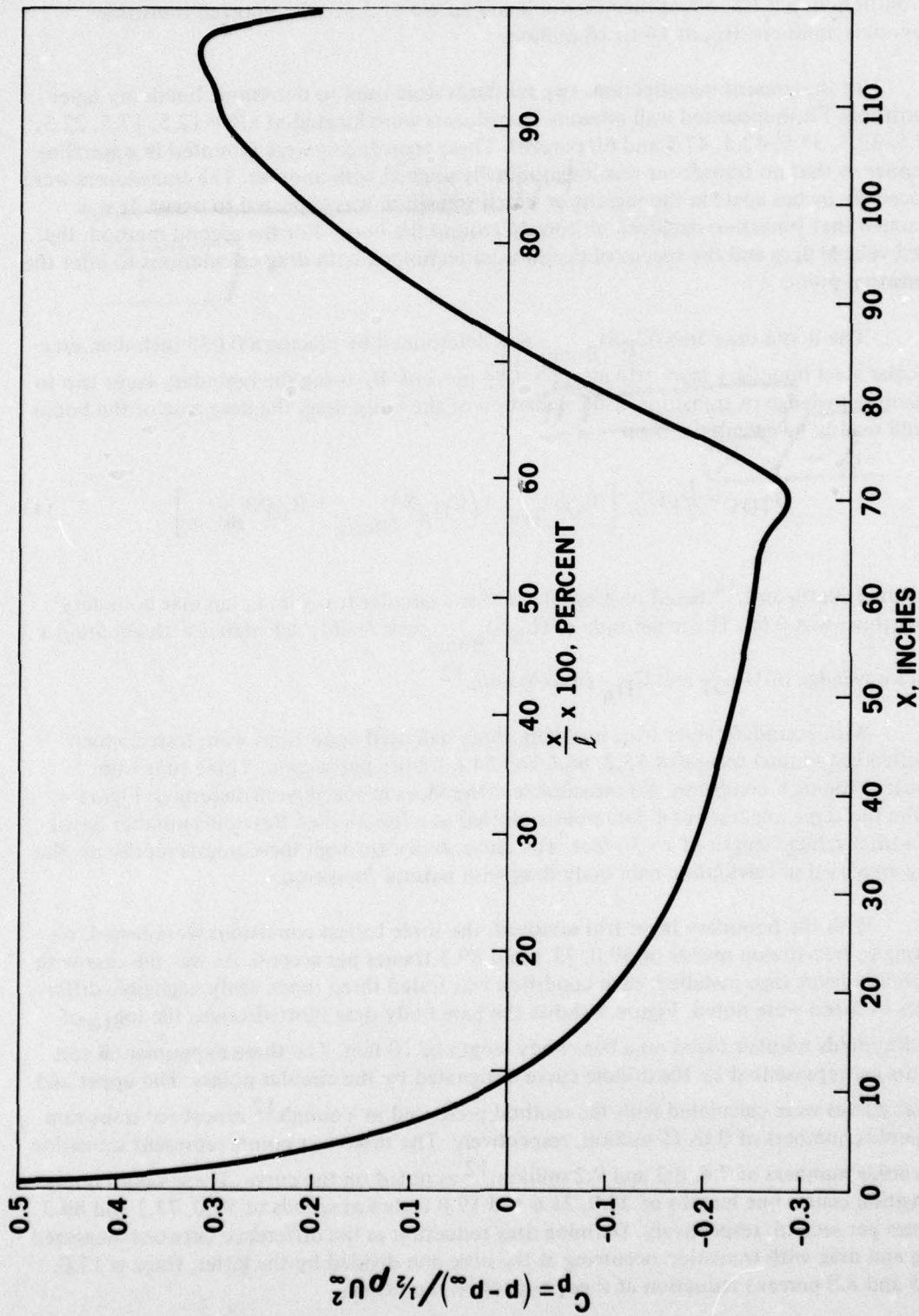Figure 2. Cylindrically shaped 15-inch-diameter vehicle (SWISH).

Figure 3. Theoretical CARROT vehicle pressure distribution.

gravity-propelled vehicle of similar shape. The body was an NACA 66 series body of revolution with a 1.575-feet-diameter hull and an ℓ/d of 3.33. He reported transition Reynolds numbers, R_x, of 14 to 18 million.

In the present investigation, two methods were used to determine boundary layer transition. Flush-mounted wall-pressure transducers were located at $x/\ell = 12.5, 17.5, 22.5, 27.5, 32.5, 37.5, 42.5, 47.5$ and 60 percent. These transducers were mounted in a spiraling manner so that no transducer was longitudinally aligned with another. The transducers were spaced six inches apart in the regions in which transition was expected to occur. It was assumed that transition occurred uniformly around the body. For the second method, the total vehicle drag and the speeds obtained were combined with drag calculations to infer the transition point.

The boom drag area $(C_D S)_{Boom}$ was determined by placing a 0.035-inch-diameter circular steel boundary layer trip at $x/\ell = 4.84$ percent. By using the boundary layer trip to ensure knowledge of transition and calculation of the body drag, the drag area of the boom could readily be calculated from

$$D_{TOT} = \frac{1}{2}\rho U_\infty^2 \left[(C_D S)_{Trip} + \left(C_{D_A} S \right)_{Body} + (C_D S)_{Boom} \right] \tag{1}$$

The drag coefficient,[14] based on frontal area for a circular trip wire in laminar boundary layer flow, was 0.65. The magnitude of $(C_D S)_{Boom}$ was readily calculated with equation 1 and knowledge of D_{TOT} and C_{D_A} from Young.[12]

With boundary layer trips installed, three ballasted conditions were tested which resulted in terminal speeds of 55.2, 68.6 and 84.6 frames per second. Three runs were repeated for each condition. No measurable differences in speed were discerned. Figure 4 shows the three experimental data points plotted as a function of Reynolds number based on a total vehicle length of 15.36 feet. The curve drawn through these points represents the drag area used in calculating bare body drag with natural transition.

With the boundary layer trip removed, the three ballast conditions were tested, resulting in free-stream speeds of 59.0, 73.1 and 89.3 frames per second. As was the case with boundary layer trips installed, each condition was tested three times. Only negligible differences in speed were noted. Figure 5 shows the bare body drag plotted versus the $\log_{10}$ of the Reynolds number based on a bare body length of 10 feet. The three experimental test points are represented by the middle curve designated by the circular points. The upper and lower curves were calculated with the method presented in Young's[12] report for transition Reynolds numbers of 0 to 15 million, respectively. The three test points represent transition Reynolds numbers of 7.4, 8.2 and 9.2 million,[12] as noted on the curve. These values imply transition center line lengths of 24.0, 21.6 and 19.8 inches at speeds of 59.0, 73.1 and 89.3 frames per second, respectively. Defining drag reduction as the difference between measured drag and drag with transition occurring at the nose and divided by the latter, there is 13.0, 10.5 and 8.8 percent reduction at these respective conditions.
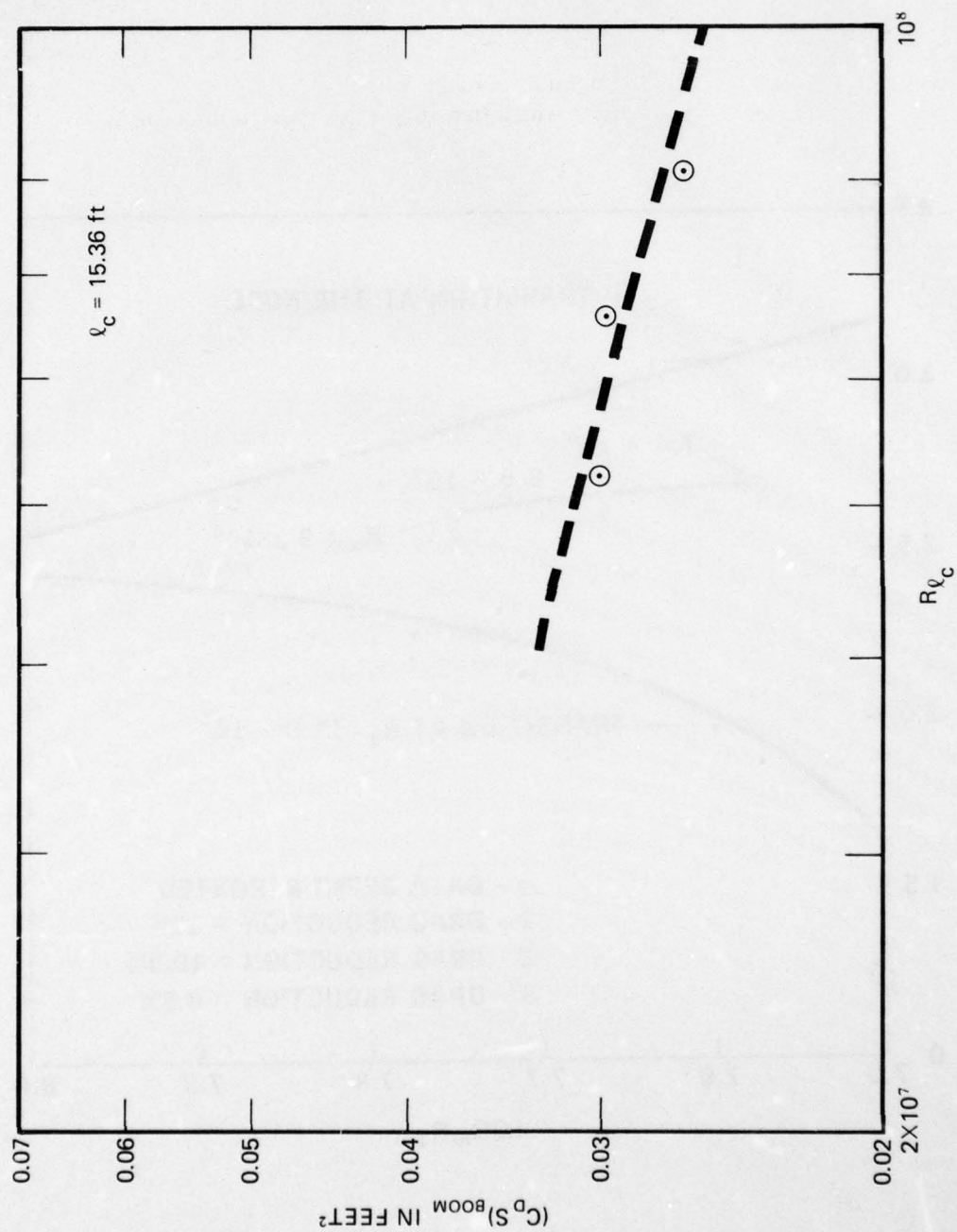
8

Figure 4. CARROT boom drag area.

$\ell_c = 15.36$ ft

$R\ell_c$
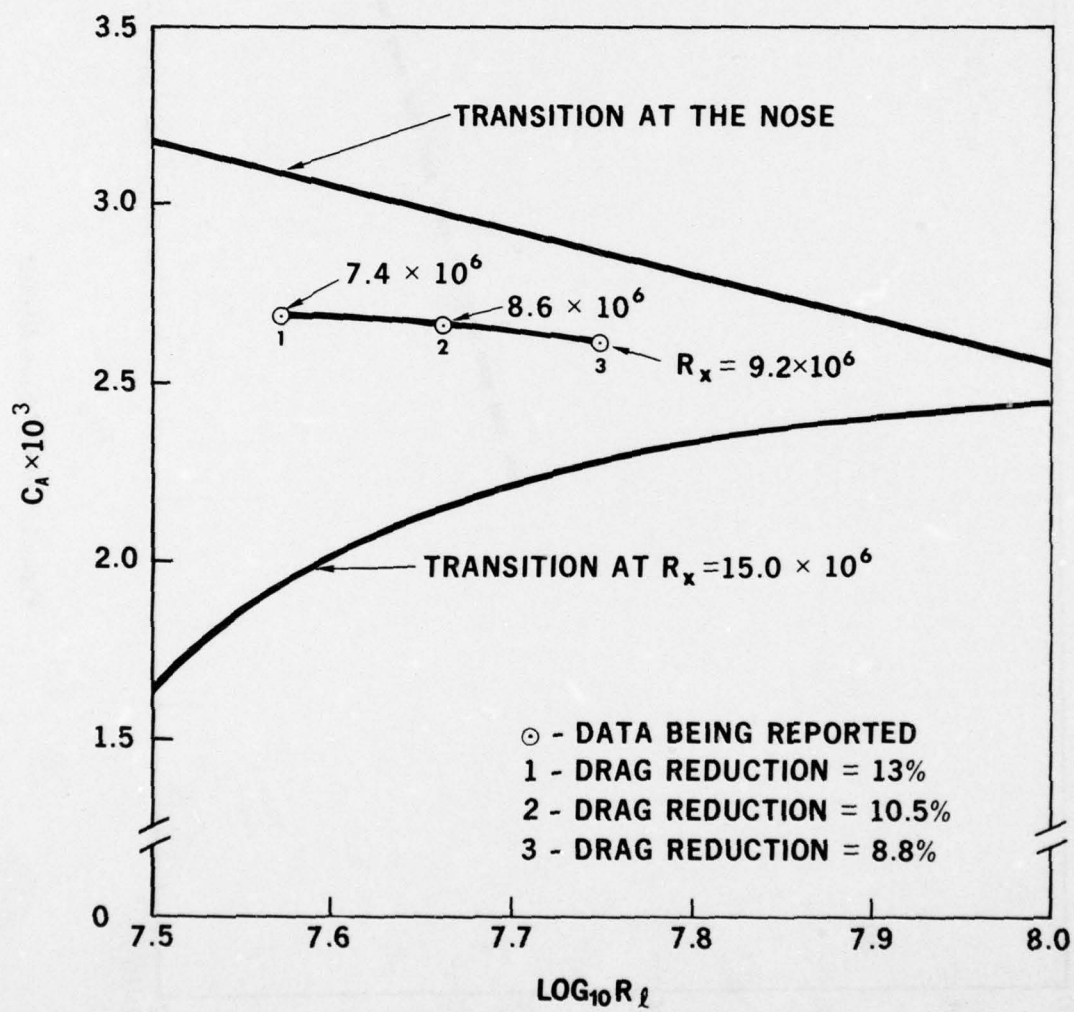
$(C_D S)_{BOOM}$ IN FEET²

9

Figure 5. CARROT bare body drag.

These calculated transition lengths agree with the flush-mounted pressure transducer information. Turbulent boundary flow was indicated by the greatly increased magnitude of the transducer output when compared to transducers in the laminar flow region. The transducer mounted at x = 27 inches indicated turbulent flow and another at x = 21 inches indicated laminar flow at speeds of 59.0 and 73.1 frames per second. When U_∞ was 89.3 frames per second, turbulent flow was found at x = 21 inches and laminar flow at x = 15 inches.

Transition from laminar to turbulent boundary layer flow is a function of pressure gradient, skin roughness, free-stream turbulence and surface waviness. The transition Reynolds numbers reported are approximately one-half those measured by Carmichael[13] using a body with similar pressure gradients and skin smoothness. As previously noted, surface waviness was not measured on the CARROT vehicle. It is reasonable, therefore, to hypothesize that the differences in R_x are due to higher levels of waviness on the body being reported.

PRESSURE GRADIENT EFFECTS ON BOUNDARY LAYER CHARACTERISTICS

The pressure gradient of the CARROT vehicle, which is shown in Figure 3, could possibly alter the boundary layer characteristics from those developed on flat plates. Clauser[10] has shown that relatively mild pressure gradients can significantly change C_f. Schloemer[1] found that $\Phi(\omega)$ normalized was increased at low dimensionless frequencies in adverse pressure gradients and a decrease at high frequencies was noted in favorable pressure gradients. The SWISH pressure gradient is shown in Figure 6; in the region of the transducer (x/ℓ = 49.6 percent) and for many boundary layer thickness upstream, the pressure gradient is zero.

A favorable (negative) pressure gradient exists on the CARROT body up to x/ℓ = 58 percent. Flush-mounted wall-pressure transducer measurements were analyzed in regions of favorable pressure gradient at x/ℓ = 27.5, 37.5 and 47.5 percent and in a region of unfavorable dp/dx at x/ℓ = 60 percent.

Pertinent boundary layer characteristics for CARROT at the various transducer locations and free-stream speeds are listed in Tables 1 through 4. Listed in Table 5 are the corresponding SWISH characteristics. The boundary layer parameters $\delta, \delta^*, \theta, H, \tau_w, C_f$ and R_θ were calculated with the theory and computer program developed by Nelson.[15] His calculation method was shown to be accurate when the point of transition from laminar to turbulent boundary layer flow is known and when the surface finish is hydraulically smooth. Transition on SWISH was assumed to occur at x/ℓ = 2.36 percent, which was based on past experimental measurements.[8] Transition on CARROT was described in the preceding section. The laminar boundary layer characteristics were calculated with Pohalhausen's approximate method extended by Tomotika[16] to the case for bodies of revolution. The surface of the vehicles was maintained at a high degree of smoothness. Because of the care

11
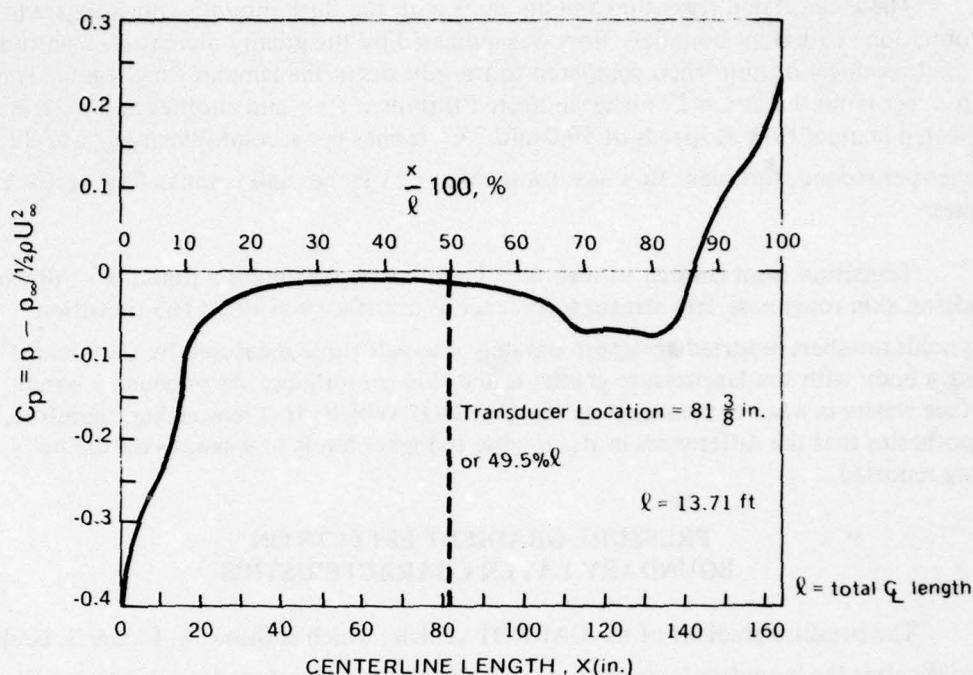
Figure 6. Theoretical SWISH vehicle pressure distribution.

taken in handling the vehicles as well as the proven reliability of past calculations, the boundary layer parameters presented are believed to be reasonably accurate.

Also presented in Tables 1 through 4 are the boundary layer shape factor G and the pressure gradient parameters π and β. Nash[17] presents an empirical relation between G and π data, as well as the theoretical relationship given by:

$$C = 6.1 (\pi + 1.81)^{1/2} - 1.7 . \tag{2}$$

For a flat plate or SWISH at x/ℓ = 49.6 percent, π is zero and G = 6.5 when based on Equation 2. For SWISH G = 6.77 to 6.79, which agrees reasonably well with Equation 2. It was shown that G = 6.77 to 6.79 for CARROT at all locations and speeds which indicates that G was very similar to SWISH and therefore similar to flat plate measurements.

In the regions of favorable pressure gradient on CARROT (Tables 1 through 3), π = –0.0293 to –0.0459, and in the adverse region (Table 4) π = 0.328 to 0.335. It is felt that these are insignificantly different from zero, because substitution of these values of π into Equation 2 results in negligible changes from G = 6.5.

Clauser[10] used the pressure gradient parameter β and plotted it as a function of H for equilibrium turbulent boundary layers for adverse pressure gradients. His results show that H = 1.28 to 1.45 for $\beta \approx 0$. For both SWISH and CARROT at all test conditions, H varied from 1.279 to 1.340. Nelson[15] has also shown that H is dependent on R_θ.

12

Table 1. CARROT Body Turbulent Boundary Layer
Characteristics at $x/\ell = 27.5$ percent.

U_∞(ft/sec)	89.3	73.1	59.0
U_∞(cm/sec)	2721	2228	1798
δ (cm)	0.476	0.456	0.403
δ^* (cm)	0.0625	0.0608	0.0553
θ (cm)	0.0474	0.0458	0.0413
H	1.318	1.327	1.340
τ_w(dyne/cm^2)	11.14×10^3	7.80×10^3	5.38×10^3
C_f	2.54×10^{-3}	2.65×10^{-3}	2.81×10^{-3}
R_θ	9.05×10^3	7.16×10^3	5.21×10^3
G	6.77	6.77	6.77
π	-0.0365	-0.0341	-0.0293
β	-0.0277	-0.0257	-0.0219

13

Table 2. CARROT Body Turbulent Boundary Layer
Characteristics at x/ℓ = 37.5 percent.

U_∞(ft/sec)	89.3	73.1	59.0
U_∞(cm/sec)	2721	2228	1798
δ (cm)	0.797	0.780	0.749
δ^* (cm)	0.0997	0.0993	0.0974
θ (cm)	0.0767	0.0760	0.0740
H	1.300	1.307	1.316
τ_w(dyne/cm^2)	10.61×10^3	7.36×10^3	5.00×10^3
C_f	2.35×10^{-3}	2.43×10^{-3}	2.54×10^{-3}
R_θ	14.86×10^3	12.07×10^3	9.48×10^3
G	6.73	6.74	6.74
π	-0.0459	-0.0418	-0.0416
β	-0.0353	-0.0320	-0.0316

Table 3. CARROT Body Turbulent Boundary Layer
Characteristics at x/ℓ = 47.5 percent.

U(ft/sec)	89.3	73.1	59.0
U(cm/sec)	2721	2228	1798
δ(cm)	1.129	1.123	1.109
δ^*(cm)	0.1375	0.1399	0.1397
θ(cm)	0.1066	0.1072	0.1072
H	1.290	1.296	1.303
τ_W(dyne/cm^2)	10.22×10^3	7.05×10^3	4.77×10^3
C_f	2.22×10^{-3}	2.28×10^{-3}	2.37×10^{-3}
R_θ	20.9×10^3	17.19×10^3	13.86×10^3
G	6.75	6.76	6.76
π	-0.0432	-0.0424	-0.0410
β	-0.0335	-0.0327	-0.0315

15

Table 4. CARROT Body Turbulent Boundary Layer
Characteristics at $x/\ell = 60$ percent.

U_∞(ft/sec)	89.3	73.1	59.0
U_∞(cm/sec)	2721	2228	1798
δ(cm)	1.643	1.645	1.642
δ^*(cm)	0.1948	0.1978	0.201
θ(cm)	0.1522	0.1541	0.1561
H	1.279	1.284	1.290
τ_W(dyne/cm^2)	10.00×10^3	6.86×10^3	4.61×10^3
C_f	2.12×10^{-3}	2.17×10^{-3}	2.24×10^{-3}
R_θ	30.2×10^3	25.0×10^3	20.4×10^3
G	6.70	6.71	6.72
π	0.335	0.333	0.328
β	0.309	0.259	0.254

16

Table 5. SWISH Body Turbulent Boundary Layer Characteristics.

U_∞ (ft/sec)	67.1	63.1	48.0
U_∞ (cm/sec)	2044	1923	1463
δ (cm)	2.67	2.63	2.75
δ^* (cm)	0.323	0.325	0.341
θ (cm)	0.253	0.254	0.265
H	1.279	1.280	1.287
τ_w (dyne/cm^2)	4.36×10^3	3.90×10^3	2.34×10^3
C_f	2.07×10^{-3}	2.09×10^{-3}	2.16×10^{-3}
R_θ	33.5×10^3	31.7×10^3	25.1×10^3
G	6.78	6.77	6.79

Schloemer[1] reported significant changes in normalized $\Phi(\omega)$ for $\beta \approx 2.1$ (H = 1.58) and $\beta \approx -0.22$ (H = 1.35-1.36) in two-dimensional wind tunnel tests. Both of these favorable and unfavorable pressure gradient parameters were an order of magnitude greater than those presently being reported.

It is reasonable to compare the CARROT to SWISH data with flat plate experiments because the pressure gradients were of such small magnitude. A possible exception might be for the CARROT transducer located at $x/\ell = 60$ percent, which is in an adverse pressure gradient region. Inspection of Figure 3 in this area shows that dp/dx is rapidly changing. The effect of d^2p/dx^2 may be a significant parameter even though the pressure gradient appears to be negligible.

WALL-PRESSURE POWER SPECTRAL DENSITY

The boundary layer thickens as x increases; therefore, the wall-pressure fluctuation measured on CARROT will be at different δ^* at a given free-stream speed. Corcos[18] has shown that $\Phi(\omega)$ is attenuated as d increases because of the finite size of the transducer. This phenomenon is obvious, as shown in Figure 7, since $10 \, \mathrm{Log}_{10}\left[\Phi(\omega)/\rho^2 U_\infty^3 \delta^*\right]$ is plotted as a function of dimensionless frequency $\omega\delta^*/U_\infty$. Table 6 presents the symbols used for plotting normalized $\Phi(\omega)$ and will be used in all the figures presented. The table shows that, on CARROT, as x/ℓ increases, d/δ^* decreases and at a given x/ℓ, d/δ^* does not significantly change over the speed range tested (59.0 to 89.3 frames per second). The curve in Figure 7 for $d/\delta^* = 1.0$ represents SWISH measurements and for $d/\delta^* = 1.6, 2.3, 3.2$ and 5.3 represents CARROT data at $x/\ell = 60$ percent, 47.5 percent, 37.5 percent and 27.5 percent, respectively. Also shown on Figure 7 is Bakewell's[9] data for $d/\delta^* = 0.6$ to 0.7, which were measured on a body of revolution in water. It is quite clear that as d/δ^* increases, the normalized $\Phi(\omega)$ is increasingly attenuated at high dimensionless frequencies. It is also clear that the transducer resolution improves as $\omega\delta^*/U_\infty$ decreases.

A theoretical correction for flush-mounted transducers has been developed by Corcos.[18] The attenuation increases for increasing ω at a given d and U_∞; it is clear that d must be very small to obtain measurements that are not drastically attenuated. Willmarth,[2] Kirby[5] and others have shown that Corcos's correction is not completely valid because d/δ^* has been verified experimentally to constitute a transducer resolution parameter. Corcos's correction appears to be valid when d/δ^* is relatively small and $\omega\delta^*/U_\infty$ is not large. Previous investigations[19] have shown that for the transducer used in the present investigation (d = 0.125 inches) and for $d/\delta^* = 1.0$, Corcos's correction wasn't applicable over most of the high dimensionless frequency range. Because of the apparent unapplicability of Corcos's correction to the present investigation, it will not be used.

In Figure 7 all points representing different speeds are shown to fall closely together, forming a group of d/δ^* curves. The lowest curve represents $d/\delta^* = 5.3$; as d/δ^* decreases, the representative curves increase in magnitude until $d/\delta^* = 1.0$, which represents the lowest d/δ^* being reported. The dashed curve for $d/\delta^* = 0.6$ to 0.7 represents Bakewell's[9] water

18

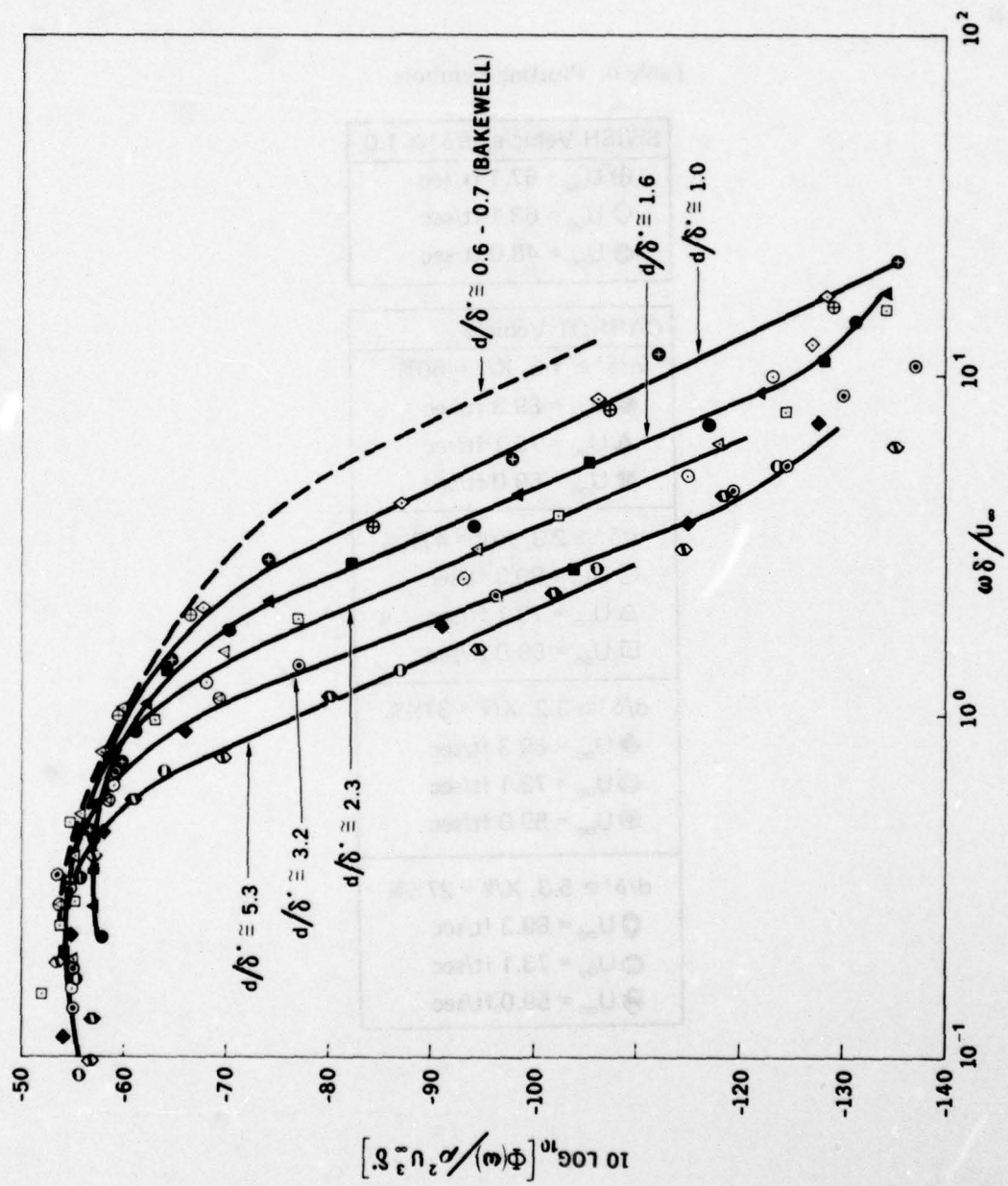Figure 7. Normalized (re: 2q and δ*) wall pressure spectral density.

Table 6. Plotting Symbols.

SWISH Vehicle, $d/\delta^* \cong 1.0$
$\oplus\ U_\infty = 67.1$ ft/sec
$\Diamond\ U_\infty = 63.1$ ft/sec
$\oplus\ U_\infty = 48.0$ ft/sec

CARROT Vehicle
$d/\delta^* \cong 1.6,\ X/\ell = 60\%$
$\bullet\ U_\infty = 89.3$ ft/sec
$\blacktriangle\ U_\infty = 73.1$ ft/sec
$\blacksquare\ U_\infty = 59.0$ ft/sec
$d/\delta^* \cong 2.3,\ X/\ell = 47\frac{1}{2}\%$
$\odot\ U_\infty = 89.3$ ft/sec
$\triangle\ U_\infty = 73.1$ ft/sec
$\square\ U_\infty = 59.0$ ft/sec
$d/\delta^* \cong 3.2,\ X/\ell = 37\frac{1}{2}\%$
$\blacklozenge\ U_\infty = 89.3$ ft/sec
$\oslash\ U_\infty = 73.1$ ft/sec
$\odot\ U_\infty = 59.0$ ft/sec
$d/\delta^* \cong 5.3,\ X/\ell = 27\frac{1}{2}\%$
$\ominus\ U_\infty = 89.3$ ft/sec
$\ominus\ U_\infty = 73.1$ ft/sec
$\ominus\ U_\infty = 59.0$ ft/sec

20

measurements and is in accord with the parametric curves. At $\omega\delta^*/U_\infty < 0.5$, all of the curves fall closely together, except for $d/\delta^* = 1.6$. This low dimensionless frequency range corresponds to the region in which the transducer attenuation is negligible. At these low $\omega\delta^*/U_\infty$, the curve representing $d/\delta^* = 1.6$ constitutes the CARROT measurements at $x/\ell = 60$ percent, which was the point at which d^2p/dx^2 was large. This region of rapidly changing pressure gradient may be the reason why the $d/\delta^* = 1.6$ doesn't collapse to the single curve. At $\omega\delta^*/U_\infty < 2$ the $d/\delta^* = 1.0$ (SWISH) data are identical to Bakewell's $d/\delta^* \approx 0.6$ to 0.7 curve, which shows that the two curves are alike except for the transducer attenuation at $\omega\delta^*/U_\infty > 2$.

It is also possible to normalize $\Phi(\omega)$ with the wall shear stress τ_w as the character-istic pressure term. The method is heuristically more logical because τ_w describes a boundary layer characteristic at the transducer location and not free-stream conditions. Because of the difficulty in measuring τ_w, it was calculated by the method described earlier; the values are listed in Tables 1 through 5. Figure 8 gives the wall-shear-stress normalization, with $10 \, Log_{10} \left[\Phi(\omega) U_\infty / \tau_w^2 \delta^* \right]$ plotted versus $\omega\delta^*/U_\infty$. Again, a family of d/δ^* parametric curves is found from a description of magnitude with increasing d/δ^*. This method of normalizing is not as effective as the previous one because of the low $\omega\delta^*/U_\infty$. The SWISH curve $d/\delta^* = 1.0$ is greater in magnitude than the CARROT ($d/\delta^* = 1.6$ to 5.3). Also shown are two dashed curves representing Willmarth's[2] flat plate data in air and $d/\delta^* \approx 0.44$ and Kirby's[5] rotating cylinder in water data and $d/\delta^* = 2$ to 3. At low $\omega\delta^*/U_\infty$ both dashed curves are shown to be greater in magnitude than either the CARROT or SWISH data. This discrepancy is either due to inaccuracies in calculating τ_w or to the un-applicability of the normalizing technique. Willmarth's curve represents approximately an upper limit of the family of parametric curves except that the slope of high $\omega\delta^*/U_\infty$ is less than those being reported. Kirby's curve is fundamentally different from those being reported because of the change in slope at $\omega\delta^*/U_\infty \approx 2.5$ and the curve is considerably greater in magnitude than the data reported for equivalent d/δ^*. This latter discrepancy may be due to the fundamental differences in viscous flow on rotating cylinders as com-pared to turbulent boundary layers developed on flat plates as noted by Coles.[20]

Foxwell[4] proposed a method of normalizing $\Phi(\omega)$ which might collapse all data to a single curve no matter what size transducer was used for the measurements. He proposed that transducer diameter be used as the characteristic length and, therefore, collapse all data at high dimensionless frequency because of the finite transducer effect. His method of normalizing was used on the data being reported and is shown in Figure 9, where $10 \, Log_{10}$ $\left[\Phi(\omega) U_\infty / \tau_w^2 d \right]$ is plotted as a function $\omega d/U_\infty$. The solid curve depicts the experimental data and the dashed curve represents Foxwell's theoretical curve at high frequencies, which is primarily based on data with rotating cylinders in water.

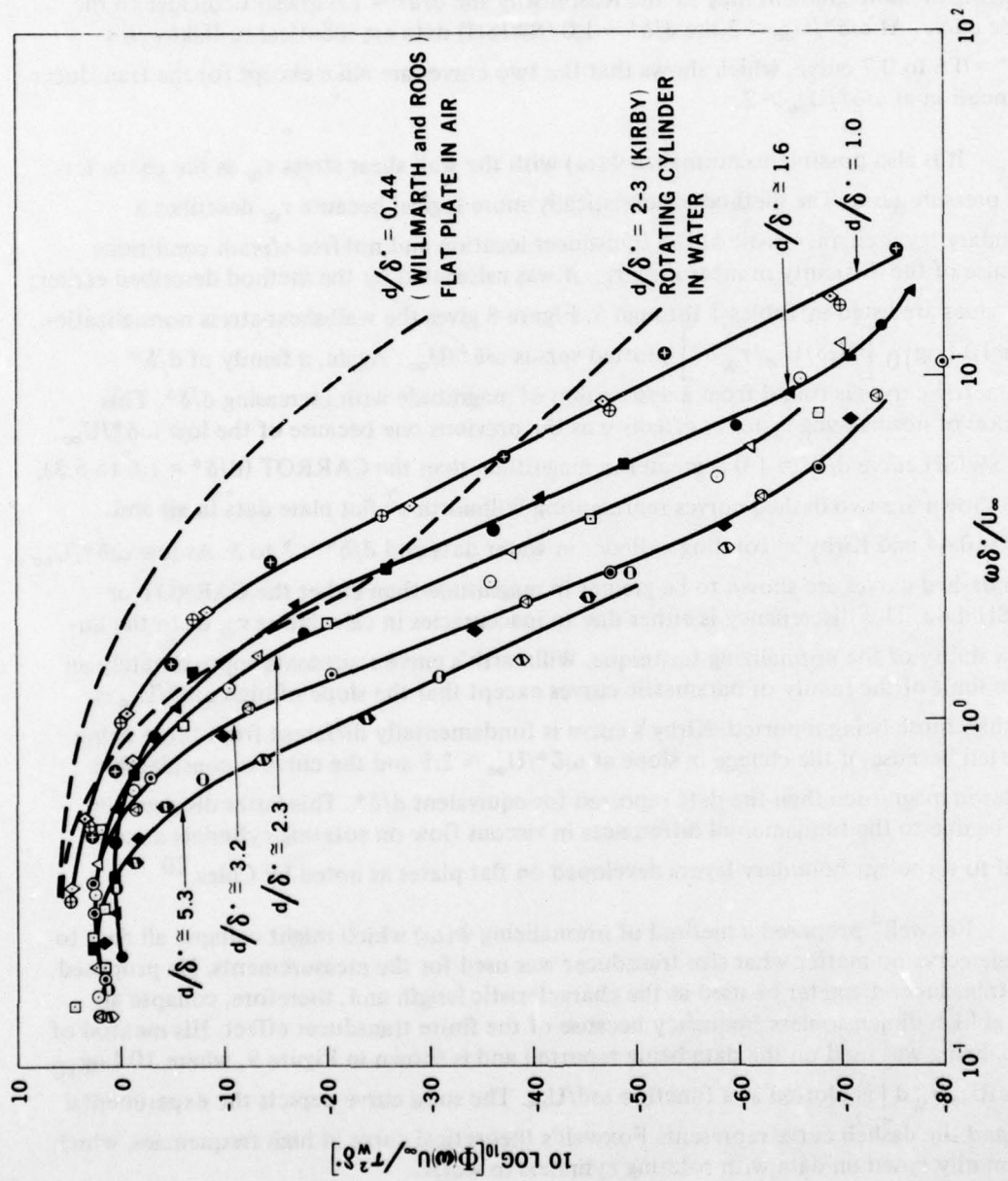Figure 8. Normalized (re: τ_w and δ^*) wall pressure spectral density.

22

FOXWELL'S THEORETICAL CURVE

$10 \, LOG_{10} \left[\Phi(\omega) U_\infty / \tau_w^2 \, d \right]$
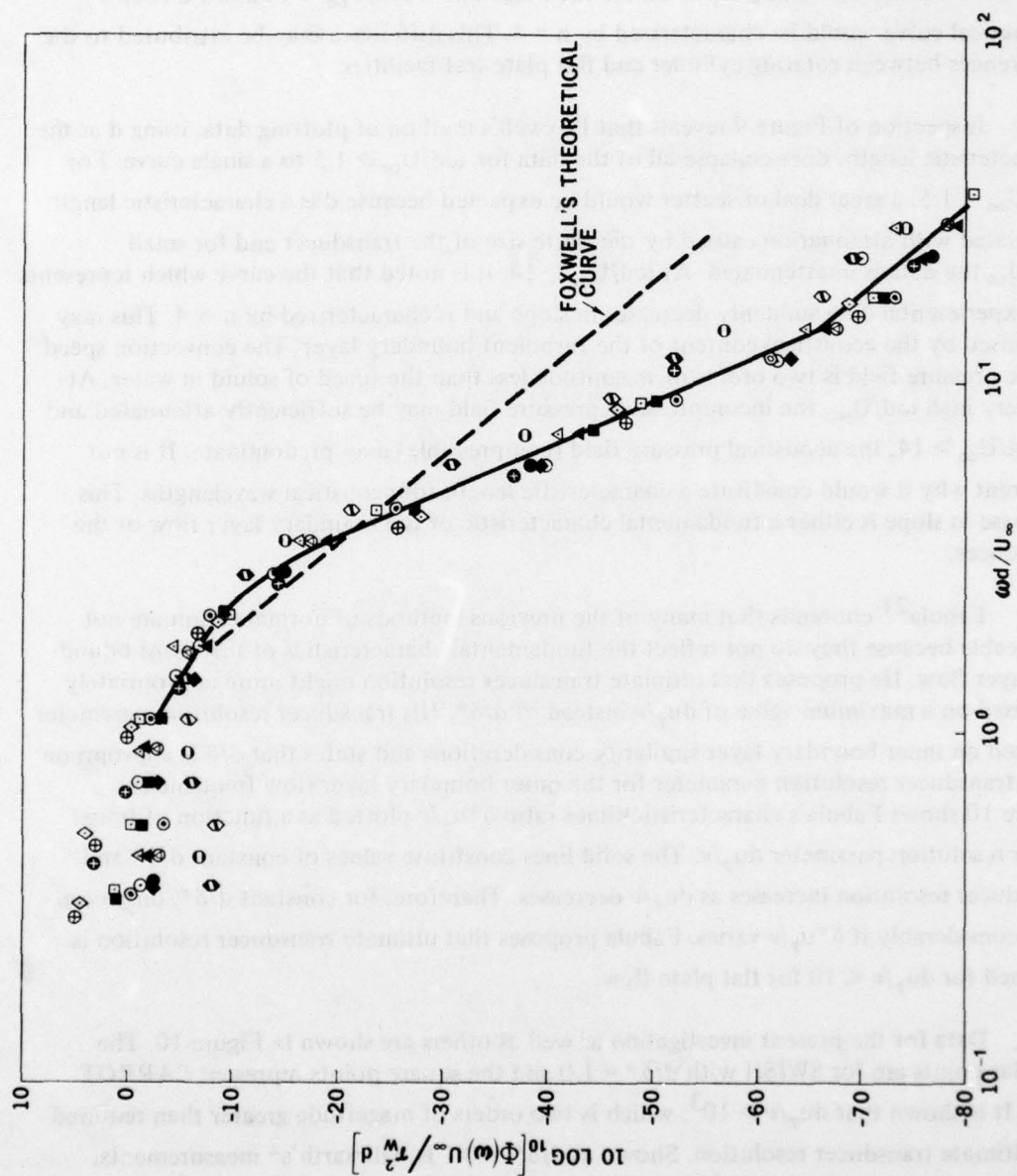
$\omega d / U_\infty$

Figure 9. Normalized (re: τ_w and d) wall pressure spectral density.

If it is assumed that the normalized power spectrum at high frequencies is proportional to the dimensionless frequency raised to the minus n power:

$$\left[\Phi(\omega)U_\infty/\tau_w^2 \, d \quad \propto \quad \omega d/U_\infty\right]^{-n},\qquad (3)$$

then n = 7 for the data being reported for the range $3.5 \leqslant \omega d/U_\infty \leqslant 14$ and Foxwell's theoretical curve would be characterized by n = 4. This difference may be attributed to the differences between rotating cylinder and flat plate test facilities.

Inspection of Figure 9 reveals that Foxwell's method of plotting data, using d as the characteristic length, does collapse all of the data for $\omega d/U_\infty > 1.5$ to a single curve. For $\omega d/U_\infty < 1.5$, a great deal of scatter would be expected because d is a characteristic length associated with attenuation caused by the finite size of the transducer and for small $\omega d/U_\infty$ the data is unattenuated. At $\omega d/U_\infty > 14$, it is noted that the curve which represents the experimental data suddenly decreases in slope and is characterized by n ≈ 4. This may be caused by the acoustical content of the turbulent boundary layer. The convection speed of the pressure field is two orders of magnitude less than the speed of sound in water. At the very high $\omega d/U_\infty$, the incompressible pressure field may be sufficiently attenuated and at $\omega d/U_\infty > 14$, the acoustical pressure field (compressible) may predominate. It is not apparent why d would constitute a characteristic length for acoustical wavelengths. This decrease in slope is either a fundamental characteristic of the boundary layer flow or the transducer.

Fabula[21] contends that many of the previous methods of normalization are not applicable because they do not reflect the fundamental characteristics of turbulent boundary layer flow. He proposes that ultimate transducer resolution might more appropriately be based on a maximum value of du_τ/ν instead of d/δ^*. His transducer resolution parameter is based on inner boundary layer similarity considerations and states that d/δ is appropriate for a transducer resolution parameter for the outer boundary layer (low frequencies). Figure 10 shows Fabula's characteristic-times ratio δ^*u_τ/ν plotted as a function of transducer resolution parameter du_τ/ν. The solid lines constitute values of constant d/δ^* and transducer resolution increases as du_τ/ν decreases. Therefore, for constant d/δ^*, du_τ/ν can vary considerably if δ^*u_τ/ν varies. Fabula proposes that ultimate transducer resolution is attained for $du_\tau/\nu \leqslant 10$ for flat plate flow.

Data for the present investigation as well as others are shown in Figure 10. The circular points are for SWISH with $d/\delta^* = 1.0$ and the square points represent CARROT data. It is shown that $du_\tau/\nu > 10^3$, which is two orders of magnitude greater than required for ultimate transducer resolution. Shown at $d/\delta^* \approx 0.1$ is Willmarth's[2] measurements, where $du_\tau/\nu \approx 200$ and Blake's[22] data, where $du_\tau/\nu \approx 40$ to 80. Therefore, for equal d/δ^*, Blake's data is considerably less affected by transducer attenuation than Willmarth's.
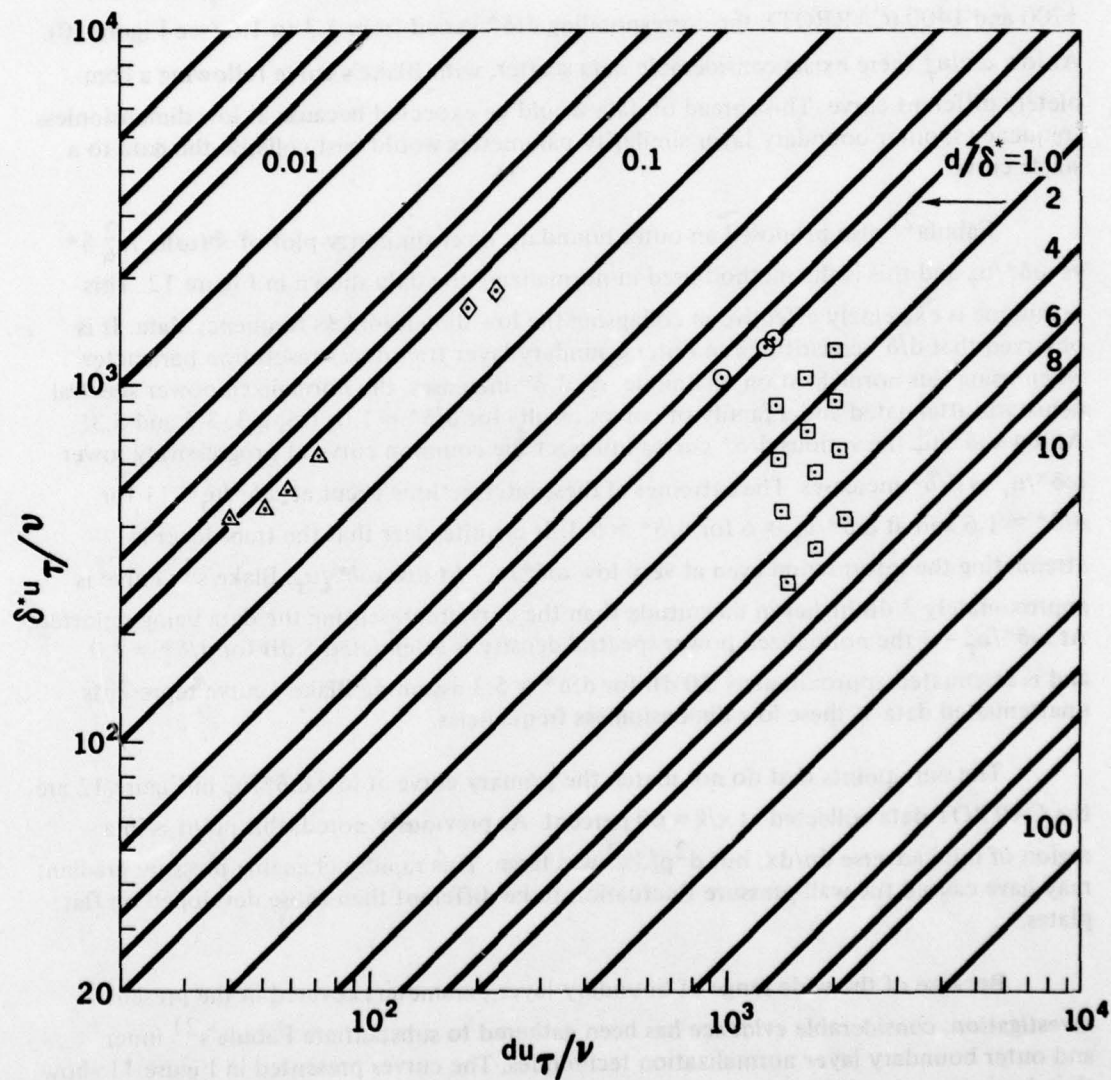
24

Figure 10. Test values of $\delta^* U_T/\nu$ and dU_T/ν: $\odot$ – SWISH, $\boxdot$ – CARROT, $\triangle$ – Blake, and $\diamondsuit$ – Willmarth.

Figure 11 features an inner boundary layer similarity plot of wall pressure power spectral density used by Fabula;[21] $10 \, Log_{10}\left[\Phi(\omega)u_\tau^2/\tau_w^2\nu\right]$ is plotted versus dimensionless frequency $\omega\nu/u_\tau^2$. Thus, the experimental data falls onto curves of constant du_τ/ν. Shown are curves for du_τ/ν of 2100, 1700, 1400 and 1000. Also shown are Blake's[22] data for $du_\tau/\nu \approx 40$ to 80. As du_τ/ν increases, $\Phi(\omega)u_\tau^2/\tau_w^2\nu$ decreases, which suggests that du_τ/ν is a very appropriate transducer resolution parameter since for each curve of $du_\tau/\nu = 2100$, 1700 and 1400 (CARROT), the corresponding d/δ^* varied from 5.3 to 1.6 (see Figure 10). At low $\omega\nu/u_\tau^2$ there exists considerable data scatter, with Blake's curve following a completely different curve. This spread of data would be expected because at low dimensionless frequencies, outer boundary layer similarity parameters would best collapse the data to a single curve.

Fabula[21] also proposed an outer boundary layer similarity plot of $\Phi(\omega)u_\tau/\tau_w^2\delta^*$ vs $\omega\delta^*/u_\tau$ and this is the method used in normalizing the data shown in Figure 12. This technique is extremely effective in collapsing the low dimensionless frequency data. It is observed that d/δ^* constitutes an outer boundary layer transducer resolution parameter when using this normalization technique. As d/δ^* increases, the normalized power spectral density is attenuated and a family of curves results for $d/\delta^* \equiv 1.0, 1.6, 2.3, 3.2$ and 5.3. At low $\omega\delta^*/u_\tau$ the various d/δ^* curves intersect the common curve at progressively lower $\omega\delta^*/u_\tau$ as d/δ^* increases. The extremes of these intersections occur at $\omega\delta^*/u_\tau \equiv 11$ for $d/\delta^* \approx 1.6$ and at $\omega\delta^*/u_\tau \approx 6$ for $d/\delta^* \approx 5.3$. It is quite clear that the transducer is attenuating the information even at very low $\omega\delta^*/u_\tau$. At low $\omega\delta^*/u_\tau$, Blake's[22] curve is approximately 3 dB higher in magnitude than the curve representing the data being reported. At $\omega\delta^*/u_\tau = 3$ the normalized power spectral density is attenuated 5 dB for $d/\delta^* \approx 1.0$ and is attenuated approximately 30 dB for $d/\delta^* \approx 5.3$ assuming Blake's curve represents unattenuated data at these low dimensionless frequencies.

The only points that do not match the primary curve at low $\omega\delta^*/u_\tau$ in Figure 12 are the CARROT data collected at $x/\ell = 60$ percent. As previously noted, this point is in a region of mild adverse dp/dx, but d^2p/dx^2 was large. This rapidly changing pressure gradient may have caused the wall-pressure fluctuation to be different than those developed on flat plates.

Because of the wide range of boundary layer parameters covered in the present investigation, considerable evidence has been gathered to substantiate Fabula's[21] inner and outer boundary layer normalization techniques. The curves presented in Figure 11 show that du_τ/ν is a true wall-pressure transducer resolution parameter and that d/δ^* presents only a partial picture of transducer attenuation, as shown in Figure 10.

26

$du_T/\nu \cong 40\text{-}80$ (BLAKE)

$du_T/\nu = 1400$

$du_T/\nu \cong 2100$

$du_T/\nu \cong 1700$

$du_T/\nu = 1000$

$\omega\nu/u_T^2$

$10 \, LOG_{10}\left[\Phi(\omega)u_T^2/\tau_w^2 \nu\right]$

20
10
0
-10
-20
-30
-40
-50
-60
-70

10^{-3} 10^{-2} 10^{-1} 10^0

$du_T/\nu \cong 2100$
CARROT VEHICLE, $U_\infty = 89.3$ ft/sec
● – X/ℓ = 60%
⊙ – X/ℓ = 47½%
◆ – X/ℓ = 37½%

$du_T/\nu \cong 1700$
CARROT VEHICLE, $U_\infty = 73.1$ ft/sec
▲ – X/ℓ = 60%
△ – X/ℓ = 47½%
⊕ – X/ℓ = 37½%

$du_T/\nu \cong 1400$
CARROT VEHICLE, $U_\infty = 59.0$ ft/sec
■ – X/ℓ = 60%
□ – X/ℓ = 47½%
⊙ – X/ℓ = 37½%

SWISH VEHICLE
⊕ – $U_\infty = 67.1$ ft/sec, ◇ – 63.1 ft/sec

$du_T/\nu \cong 1000$
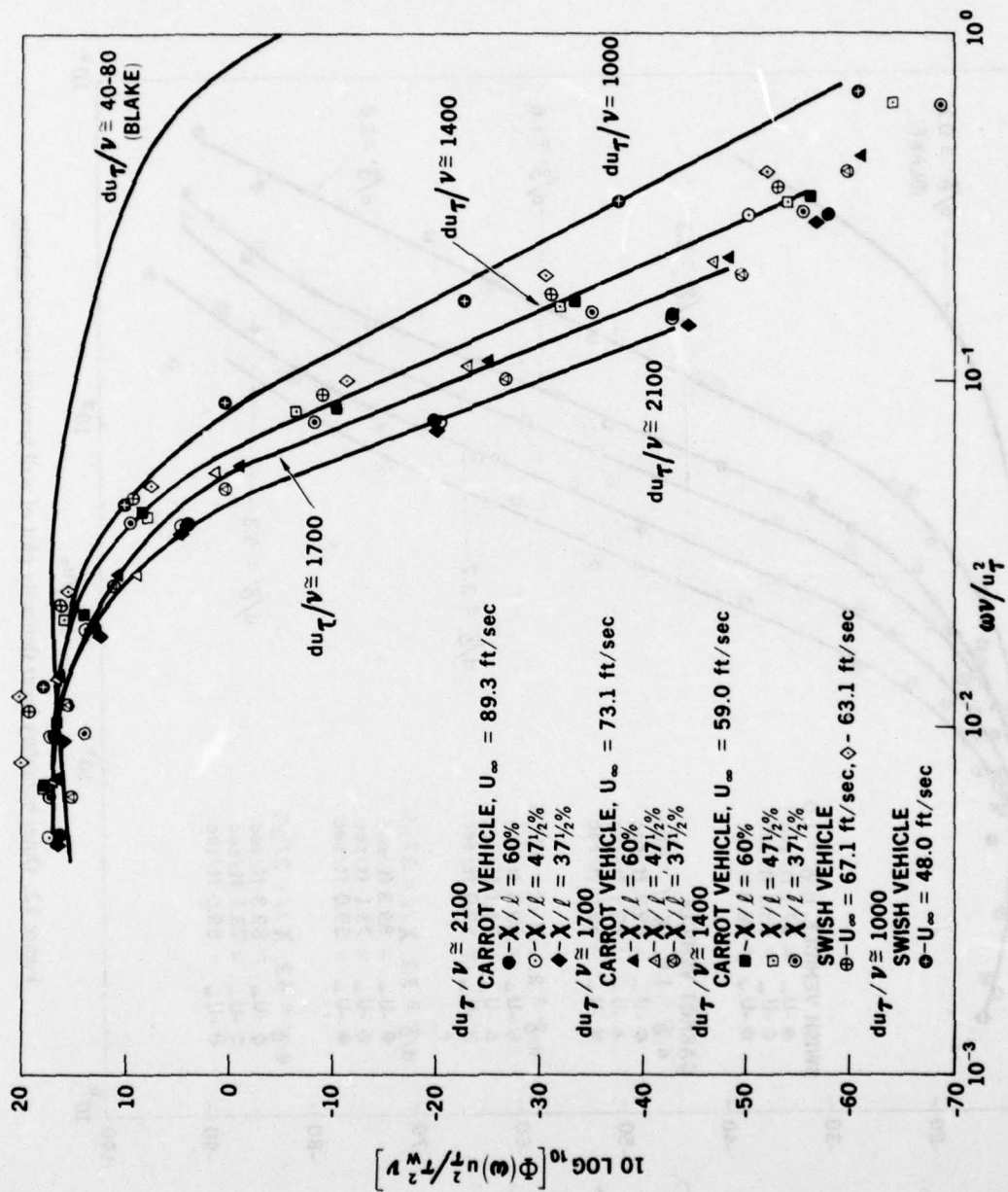SWISH VEHICLE
⊕ – $U_\infty = 48.0$ ft/sec

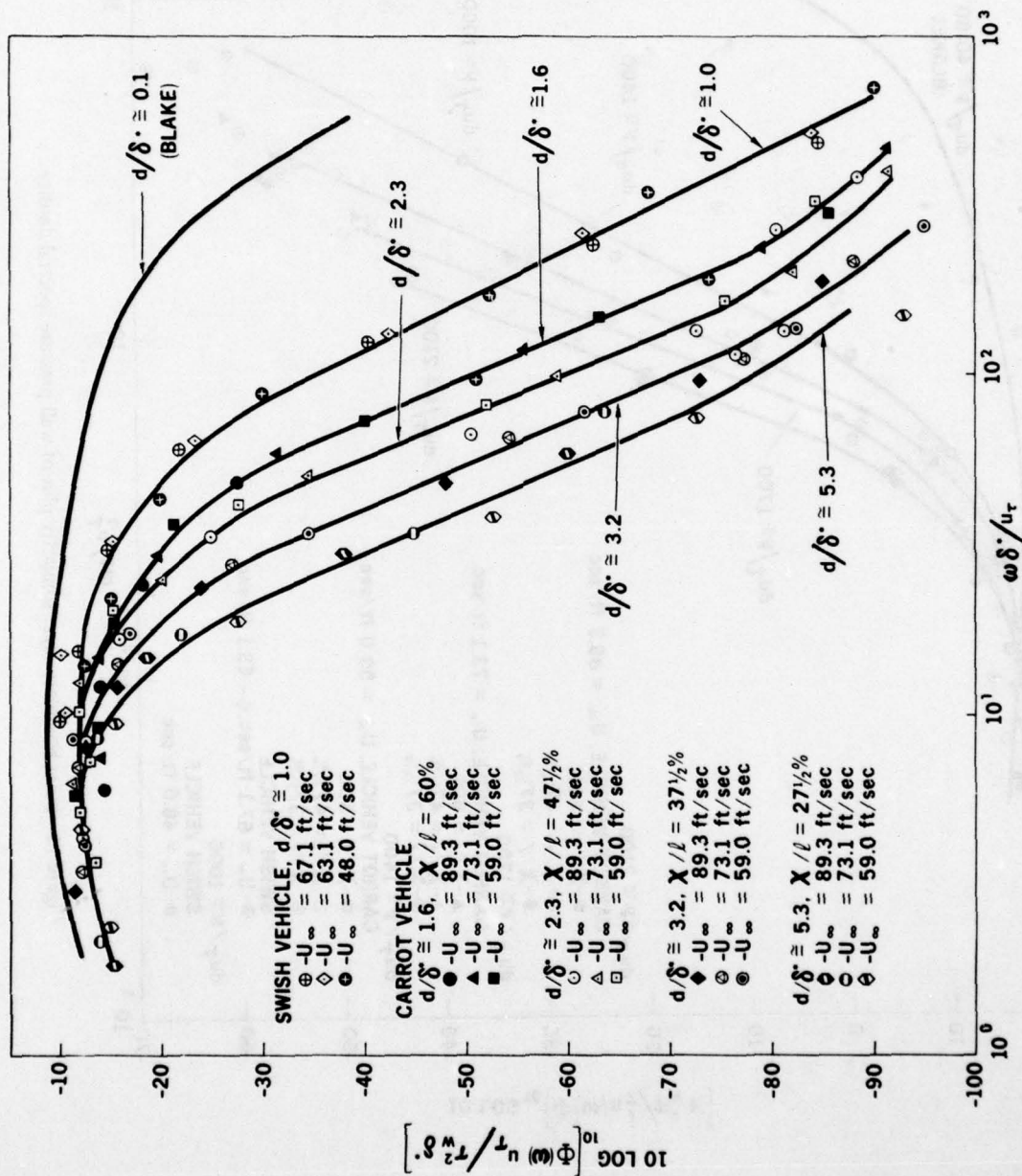Figure 11. Inner boundary layer similarity plot of wall pressure spectral density.

27

Figure 12. Outer boundary layer similarity plot of wall pressure spectral density.

CONCLUSIONS

The data of this investigation indicate that the normalized turbulent boundary layer wall-pressure fluctuations measured on a body of revolution with a mild favorable pressure gradient are in good agreement with data obtained on flat plates and cylindrical bodies with zero pressure gradients. The data suggests that du_τ/ν constitutes a more useful transducer resolution parameter than d/δ^* and that the most appropriate method of normalizing wall-pressure fluctuations should be based on inner and outer boundary layer similarity considerations. Transition from laminar to turbulent boundary layer flow occurred on the 30-inch-maximum-diameter vehicle at transition length Reynolds numbers as large as 9.2 million.

REFERENCES

1. H. H. Schloemer, "Effects of Pressure Gradients on Turbulent-Boundary-Layer Wall-Pressure Fluctuations." Journal of the Acoustical Society of America, Volume 42, Number 1, 1967.

2. W. W. Willmarth and F. W. Roos, "Resolution and Structure of the Wall Pressure Field Beneath a Turbulent Boundary Layer." Journal of Fluid Mechanics, Volume 22, Part 1, pp 81-94, 1965.

3. M. K. Bull, "Wall Pressure Fluctuations Associated with Subsonic Turbulent Boundary Layer Flow." Journal of Fluid Mechanics, Volume 28, Part 4, pp 719-754, 1967.

4. J. H. Foxwell, "The Wall Pressure Spectrum Under a Turbulent Boundary Layer." Admiralty Underwater Weapons Establishment, Portland, AUWE Technical Note 218/66, August 1966.

5. G. I. Kirby, "The Wall Pressure Spectrum of Turbulence and Its Resolution by Transducers." Admiralty Underwater Weapons Establishment, Portland, AUWE Technical Note 290-68, February 1968.

6. H. P. Bakewell, G. F. Carey, J. J. Libuha, H. H. Schloemer and W. A. Von Winkle, "Wall Pressure Correlations in Turbulent Pipe Flow." Navy Underwater Sound Laboratory, USL Report 559, August 1962.

7. G. F. Carey, J. E. Chlupsa and H. H. Schloemer, "Acoustic Turbulent Water-Flow Tunnel." Journal of the Acoustical Society of America, Volume 41, Number 2, pp 373-379, February 1967.

8. C. R. Nisewanger and F. B. Sperling, "Flow Noise Inside Boundary Layers of Buoyancy Propelled Vehicles." Naval Ordnance Test Station, NOTS TP 3511, NAVWEPS Report 8519, April 1965.

9. H. P. Bakewell, "Turbulent Wall-Pressure Fluctuations on a Body of Revolution." Journal of the Acoustical Society of America, Volume 43, Number 6, pp 1358-1363, 1968.

10. F. H. Clauser, "Turbulent Boundary Layers in Adverse Pressure Gradients." Journal of Aeronautical Sciences, Volume 21, pp 91-108, February 1954.

11. A. M. O. Smith and J. Pierce, "Calculation of Non-circulatory Plane and Axially Symmetric Flows About or Within Arbitrary Boundaries." Douglas Aircraft, Report ES 26988, April 1958.

31

12.	A. D. Young, "The Calculation of the Total and Skin Friction Drags of Bodies of Revolutions at Zero Incidence." British Research and Memorandum 1874, 27 April 1939.

13.	B. H. Carmichael, "Underwater Vehicle Drag Reduction Through Choice of Shape." American Institute of Aeronautics and Astronautics Paper Number 66-657, 1966.

14.	G. Hughes and J. F. Allen, "Turbulence Stimulation." Transactions of the Society of Naval Architects and Marine Engineers, pp 281-303, 1951.

15.	D. M. Nelson, "Turbulent-Boundary-Layer Calculations Using a Law of the Wall-Law of the Wake Method." Naval Ordnance Test Station, NOTS TP 4083, June 1966.

16.	S. Tomotika, "Approximate Methods for the Solution of the Boundary Layer Equations." <u>Boundary Layer Theory</u>, McGraw Hill, New York, 1960, Chapter XII, pp 256-258.

17.	J. F. Nash, "Turbulent-Boundary-Layer Behavior and the Auxiliary Equations." NPL Aerodynamics Report 1137, February 1965.

18.	G. M. Corcos, "Resolution of Turbulence." Journal of the Acoustical Society of America, Volume 35, Number 2, pp 192-199, February 1963.

19.	H. V. L. Patrick, Unpublished Data, April 1970.

20.	D. Cole, "Transition in a Circular Couette Flow." Journal of Fluid Mechanics, Volume 21, Part 3, pp 385-425, 1965.

21.	A. G. Fabula, Personal Communication, April 1970.

22.	W. K. Blake, "Turbulent Boundary Layer Wall Pressure Fluctuations on Smooth and Rough Walls." Massachusetts Institute of Technology, Acoustics and Vibration Laboratory, Report 70208-1, 1969.

APPENDIX

The 1/8-inch-diameter by 1/32-inch-thick barium titanate ($BaTiO_3$) crystal was coated with a two-layer watertight seal that also provided a smooth contour to the vehicle exterior. A 0.006-inch-thick Minnesota Mining and Manufacturing Company Type 471 vinyl tape was placed directly on the face of the crystal and the lip of the aluminum alloy transducer housing. The remainder of the 3/16-inch-diameter by 1/32-inch-deep cavity (total thickness of the material covering crystal surface) was filled with General Electric RTV-102 silicone rubber adhesive/sealant. Extreme care was taken to guarantee that no air bubbles were entrapped during the filling process. Air surrounded the crystal in the transverse direction to assure that there was no excitation in any other than the longitudinal direction. The physical design of the hydrophone is described in detail by Nisewanger.*

The hydrophone sensitivity level was −123 dB, re 1 V/(dyne/cm^2). The hydrophones were acoustically calibrated and the frequency response was flat within 3 dB from 100 Hz to 7 kHz. Although exact calibration at higher frequencies could not be obtained with the available facilities, there was no evidence of resonance peaks below 100 kHz.
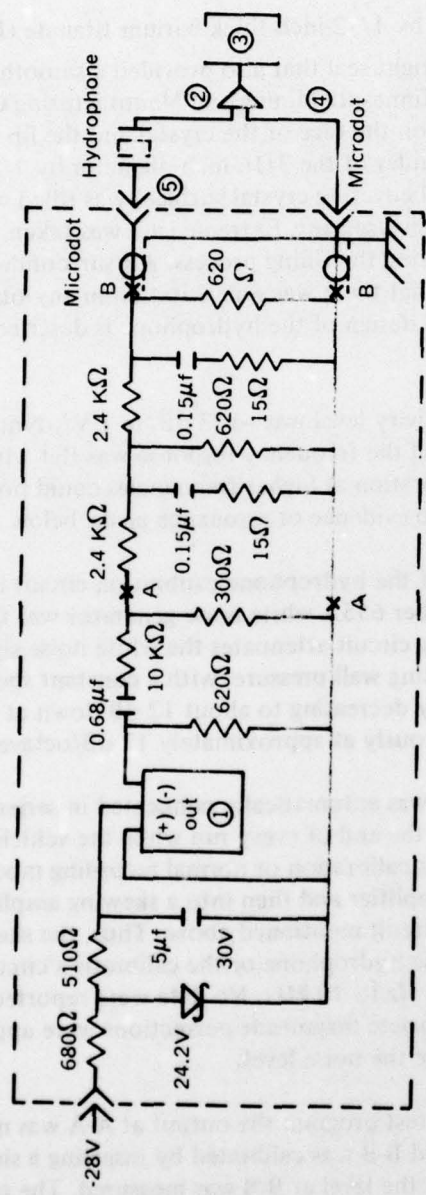
A schematic diagram of the hydrophone calibration circuit is shown in Figure A1. The output of an Allison Number 655A white noise generator was fed into a shaping circuit A-A to B-B. The shaping circuit attenuates the white noise signal so that the output at B-B is typical of the fluctuating wall pressure, with a constant spectrum level up to approximately 1 kHz, gradually decreasing to about 12 dB down at 4 kHz, after which point the level falls off continuously at approximately 12 dB/octave.

The calibration circuit was automatically connected in series with the hydrophone during the calibration phase at the end of every run while the vehicle was lying quietly on the water surface. During either calibration or normal recording modes, the signal was fed into the ITHACO fixed-gain amplifier and then into a skewing amplifier that had characteristics opposite to the shaping circuit mentioned above. Thus, the skewing amplifier conditioned the signal from either the hydrophone or the calibration circuit which was almost flat in spectrum level from 200 Hz to 40 kHz. No data were reported less than 5 dB above background noise level. Appropriate magnitude corrections were applied whenever the signal was less than 10 dB above the noise level.

Periodically during the test program the output at A-A was measured, and the shaping circuit between A-A and B-B was calibrated by inserting a sinusoidal signal at discrete frequencies at A-A and the level at B-B was measured. The circuit characteristics were always repeatable, with no changes noted throughout a three-month period.

---

*C. R. Nisewanger, "Flow Noise and Drag Measurements of Vehicle with Compliant Coating," Naval Ordnance Test Station. NAVWEPS Report 8518, NOTS TP 3510, July 1964.

33

APPENDIX

Figure A1. Noise calibration circuit.

This circuit is isolated from main chassis

① ALLISON NO. 655A WHITE NOISE GENERATOR   ④ TO GROUND ON PREAMPLIFIER

② SKEWING CIRCUIT AND ITHACO PREAMPLIFIER   ⑤ TO HYDROPHONE GROUND SIDE

③ PEMCO MAGNETIC TAPE RECORDER